Fundamental Issues and Applications of
Shock-Wave and High-Strain-Rate Phenomena
K.P. Staudhammer, L.E. Murr, and M.A. Meyers (Editors)
Published by Elsevier Science Ltd., 2001

Chapter 56

Microstructural and micromechanical aspects of ceramic/long-rod projectile interactions: dwell/penetration transitions

Jerry C. LaSalvia[a], Edward J. Horwath[a], Edward J. Rapacki[a], C. James Shih[b], and Marc A. Meyers[c]

[a]U.S. Army Research Laboratory, Aberdeen Proving Ground, MD 21005-5069
[b]Ceradyne, Inc., Costa Mesa, CA 92626
[c]University of California, San Diego, 9500 Gilman Drive, La Jolla, CA 92093

The transition from dwell to penetration by long-rod projectiles is strongly dependent upon the inelastic response of both the projectile and target materials to the stresses generated. For thick ceramic targets, the possibility for either a brittle or ductile response locally, naturally leads to both lower and upper bounds in the impact velocity for the dwell/penetration transition. The existence of these bounds was recently investigated by Lundberg and co-workers. Both bounds are governed by the inelastic region formed beneath the projectile and its extension to and/or from the free surface. The formation of the inelastic regions for the upper and lower bounds are dominated by the cumulative effects of crystal plasticity and microcracking, respectively. Evidence for the latter was obtained through detailed observations within the comminuted region of several different ceramics recovered from dwell experiments conducted by Hauver and co-workers. The dominant damage mechanism within the comminuted region appeared to be the extension of wing-cracks along grain boundaries. A wing-crack model for compressive failure of brittle materials, developed by Horii and Nemat-Nasser, enables predictions for wing-crack initiation (brittle response) and/or suppression (ductile response) depending upon the ratio of the confining stress to the applied stress σ_2/σ_1, the coefficient of friction μ, and a ductility parameter Δ defined as $K_{IC}/\tau_Y\sqrt{\pi c}$, where K_{IC} is the mode I fracture toughness (short-crack), τ_Y is the shear strength of the ceramic, and 2c is the length of the pre-existing flaw. This model, when coupled with Hertz's contact theory, provides the basis for a rational explanation for the differences in the appearance of comminuted regions in different ceramics. It also provides the basis for the derivation of an expression for the dwell/penetration transition velocity that includes the effect of mechanical properties and inference to the effect of microstructure.

1. INTRODUCTION

Ceramics are attractive materials for use in armor systems because of their superior hardness and compressive strength values relative to metals. As a result, ceramics have been subjected to a multitude of ballistic and dynamic behavior investigations during the last thirty years[1-22].

One of the more promising findings of these investigations in terms of ceramic armor development has been the phenomenon known as "interface defeat" by Hauver et al.[15-16]. Interface defeat is a term used to describe the complete erosion or dwell of a long-rod projectile on a ceramic with no penetration[15-19]. However, until recently, very little had been achieved in either its application or fundamental understanding[18-19]. A major contribution to the fundamental understanding of interface defeat was recently achieved by Lundberg et al.[20-21]. Lundberg et al.[21] investigated the velocity for the transition from interface defeat to penetration (i.e. dwell/penetration transition) of both W-based and Mo subscale long-rod projectiles fired against several ceramics. For the ceramics tested and independent of the projectile material, they found two curves, an upper and lower bound, for the dwell/penetration transition. Based upon a simple analysis, they developed upper and lower bound predictions for the transition velocities. Their hypothesis was that the lower bound is determined by the critical pressure required to initiate plastic yielding below the surface in an elastic solid. Unfortunately, this is inconsistent with observations from ceramics recovered by Hauver et al.[15-16]. Most armor ceramics that have been successfully recovered exhibited a region of intense microcracking or comminution below the impact area. The shape of this region appears consistent with deviatoric stress distributions produced as a

result of contact and therefore indicates the importance of shear with respect to the failure mechanism.

Recently, a number of micromechanics-based models have been proposed for the compressive failure of ceramics at low and high strain-rates[23-28]. Many of these failure models are based upon microcracks of the wing-crack or z-crack flaw geometry[23-27]. Wing-cracks were first observed in the compressive failure (e.g. axial splitting, faulting, plastic flow) of geological materials under confining pressure[29]. Wing-cracks are cracks that extend out of the plane of the original crack in the direction of the maximum principal stress. The catalysis for the extension of the wing-cracks is the shear failure of the original crack. However, because this shear failure is resisted by confining pressure, the failure stress is pressure dependent. As will be shown in the next section, wing-cracks are one of the dominant damage mechanisms observed within the comminuted region.

The purpose of this paper is to develop a model, based upon a wing-crack model and Hertz's theory of contact, which can provide a rationale basis for the experimental results and observations of Hauver et al.[15-16], and most recently, Lundberg et al.[20-21] with respect to the dwell/penetration transition. Furthermore, because the model is physically-based, the effect of mechanical properties and inferences to the effect of microstructure is shown.

2. INTERFACE DEFEAT

Partial dwell and interface defeat was first reported by Hauver and Melani[16]. Their first experiments were reverse-ballistic experiments, where highly confined ceramic targets were launched into subscale long-rods at velocities up to 1450 m/s. Subsequent experiments were scaled-up such that normal ballistic experiments could be conducted with subscale long-rod projectiles being launched into the ceramic targets at velocities up to 2000 m/s. Because interest was more focused on the development of ceramic armor, most later experiments were conducted at 1600 m/s. Figure 1(a) is a schematic illustration showing an early confinement scheme used by Hauver et al.[15]. Figure 1(b) is an X-ray radiograph taken during a dwell experiment[15-16]. As can be seen, the projectile is dwelling on the ceramic with eroded projectile material flowing laterally between the steel cover-plate and ceramic. Using the confinement scheme shown in Figure 1(a), Hauver et al.[15-16] was able to achieve interface defeat against quarter-scale W-based long-rod projectiles impacting at 1600 m/s for armor-grade SiC, TiB_2, TiC, and WC. Interface defeat experiments using Al_2O_3 and B_4C were not successful at this velocity. Figure 1(c) shows a TiC ceramic that was recovered from a dwell experiment. The comminuted region is clearly seen, in addition to numerous macrocracks. However, not all ceramics tested exhibited this comminuted region. Figure 1(d) shows a WC ceramic that was impacted at 1600 m/s and recovered. With the exception of the macrocracks, no comminuted region is visible.

Figure 2 is a montage of micrographs taken along the center-line axis in the comminuted region for the TiC shown in Figure 1(c). Very near the surface, Figures 2(a) and 2(b), the comminuted region does exhibit microcracks. However, the grains appear to have undergone some amount of plastic deformation (i.e. flattening) relative to grains away from the impact region (see Figure 2(e)). Moving away from the surface, the severity of the microcracking increases dramatically, Figure 2(c), with individual grains exhibiting numerous fractures and cleavage cracks. Moving further away from the surface, the severity of the microcracking decreases. The microcracks are seen to be predominately limited to grain boundaries. However, the microcracking is still severe enough such that the majority of grain boundaries are debonded. As seen in Figure 2(d), the severity of the microcracking (or grain boundary debonding) continues to gradually decrease until it finally ceases. As can be seen from these micrographs, the damage mechanisms appear to be mode II microcracks and mixed-mode (i.e. mode I and II) wing-cracks that extend along the grain boundaries. The wing-cracks (two circled) can be clearly seen in Figure 2(d). Figure 2(e) shows the undamaged microstructure.

As mentioned above, Lundberg et al.[20-21] recently investigated the transition between interface defeat and penetration. They conducted a series of reverse-ballistic experiments using both W-based and Mo projectiles against highly confined B_4C, SiC, Syndie (De Beers, Inc. trade-mark for synthetic polycrystalline diamond), and TiB_2. Figure 3 shows the impact velocity transition for these ceramics as a function of their yield strengths. Both upper and lower bound curves are also shown. As can be seen, the impact velocities for the dwell/penetration transition of SiC and TiB_2 are higher than B_4C even though its yield strength is higher. Note, even

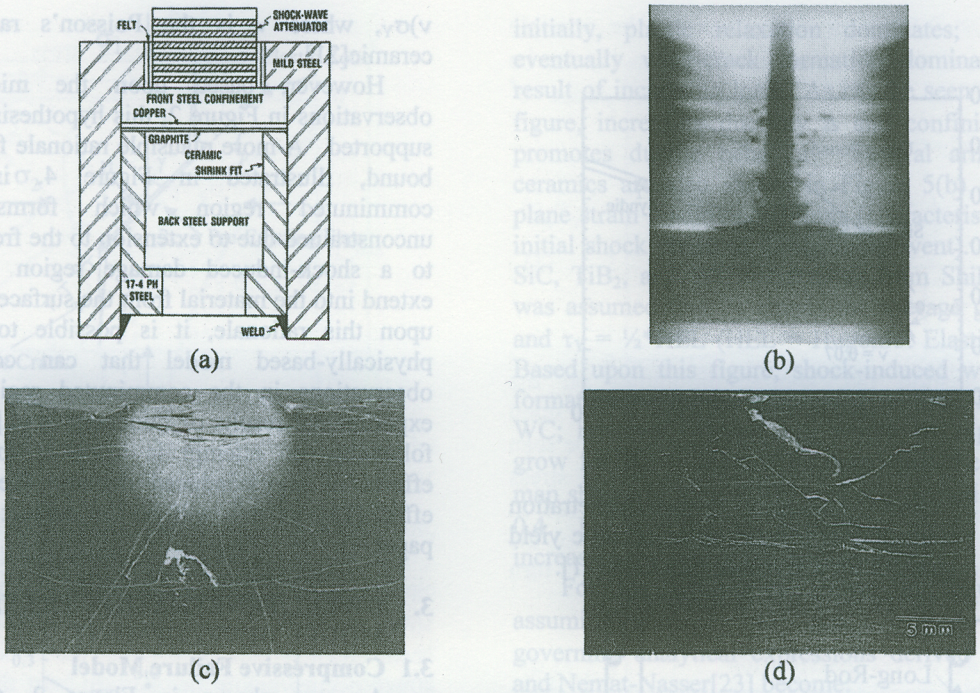

Figure 1. (a) Early ceramic confinement configuration used in ceramic dwell experiments by Hauver et al.[15]; (b) X-ray radiograph taken during dwell experiment[15-16]; (c) Polished section of ceramic (TiC) recovered after dwell experiment showing comminuted region; and (d) Polished section of WC recovered after dwell experiment showing no comminuted region.

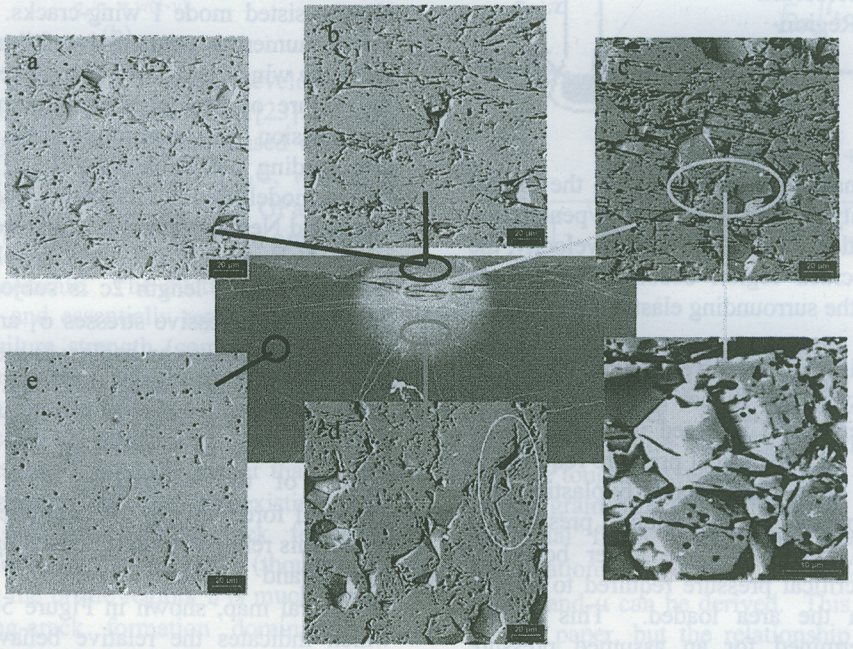

Figure 2. Comminuted region from recovered TiC. Micrographs show level of damage along the center-line axis with increasing depth.

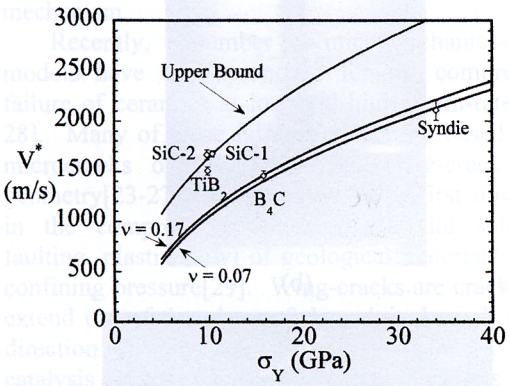

Figure 3. Impact velocity dwell/penetration transition as a function of ceramic yield strength for a W-based projectile[21].

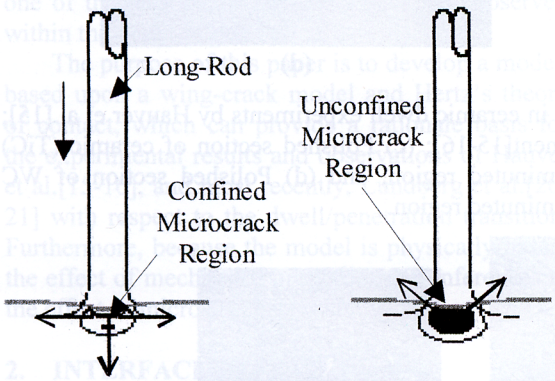

Figure 4. Rationale for lower bound in the impact velocity for the dwell/penetration transition. At critical impact velocity, the microcrack region becomes unconfined from the surrounding elastic material.

though Syndie is on the lower bound curve, its transition velocity is still higher than either SiC or TiB_2. The upper bound is based upon the plastic slip-line solution for the critical pressure required to form an indent on a rigid, perfectly-plastic body using a rigid punch. This critical pressure is approximately $2.85\sigma_Y$[30]. The lower bound is based upon the critical pressure required to initiate yielding beneath the area loaded. This critical pressure is determined for an assumed pressure distribution in combination with Boussinesq's elastic stress-field solution for a point-load on an elastic half-space. Based upon this analysis, the critical pressure for the lower bound is approximately $(1.3 + \nu)\sigma_Y$, where ν is the Poisson's ratio for the ceramic[21].

However, based upon the microstructural observations in Figure 2, this hypothesis is not well supported. A more plausible rationale for the lower bound, illustrated in Figure 4, is that the comminuted region which forms becomes unconstrained due to extension to the free surface or to a shock-induced damage region which may extend into the material from the surface[13]. Based upon this rationale, it is possible to develop a physically-based model that can correlate the observations in the comminuted region and the experimental results of Lundberg et al.[21]. In the following, no attempt is made at including the effects of shock-induced damage (i.e. strain-rate effect)[13], as this will be the subject of a future paper.

3. DWELL/PENETRATION TRANSITION MODEL DEVELOPMENT

3.1 Compressive Failure Model

As was shown in Figure 2, the damage mechanisms appear to be the extension of mode II microcracks and shear-assisted mixed-mode wing-cracks. For simplicity, it will be assumed that the predominant damage mechanism is the extension of shear-assisted mode I wing-cracks. As mentioned above, numerous compressive failure models based upon the wing-crack have been developed to explain the failure of geological and ceramic materials in compression both under quasi-static and high strain-rate loading conditions[23-27]. The compressive failure model used in this analysis was developed by Horii and Nemat-Nasser[23]. Figure 5(a) shows the wing-crack model that they developed. A pre-existing flaw of length 2c is subjected to far-field principal compressive stresses σ_1 and σ_2. The pre-existing flaw makes an angle γ as measured from the maximum principal stress direction. A plastic zone of length ℓ_p and tensile crack (wing-crack) of length ℓ_t are possible as a result of the relative motion (shear) of the pre-existing flaw surfaces. A frictional force, due to the coefficient of friction μ, resists this relative motion. Based upon their model, Horii and Nemat-Nasser[23] constructed a behavioral map, shown in Figure 5(b) for $\mu = 0.4$, which indicates the relative behavior of the pre-existing flaw as a function of a ductility parameter Δ and relative confining stress σ_2/σ_1. The ductility parameter is defined as $K_{IC}/\tau_Y\sqrt{\pi c}$, where K_{IC} is the mode I fracture toughness and τ_Y is the shear

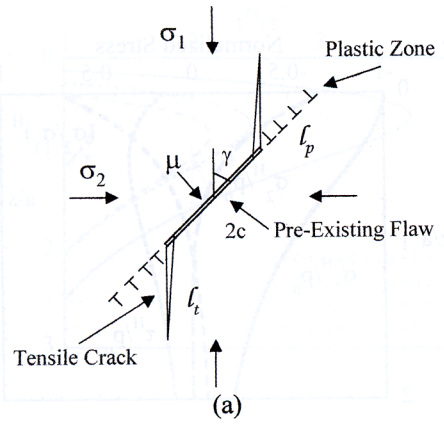

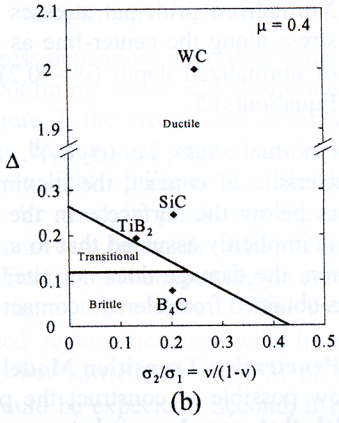

Figure 5. (a) Wing-crack model developed by Horii and Nemat-Nasser[23]. (b) Simplified ductility map based upon the wing-crack model[23]. [B_4C, $\nu = 0.17$, $K_{IC} = 2.8$ MPa$\sqrt{m}$, $\tau_Y = 8.8$ GPa (HEL = 17.6 GPa[8]), Grain size = 10 μm]

strength of the ceramic. The ductility parameter is nondimensional and essentially represents the ratio of the brittle failure strength (compressive) to the ductile failure strength. This map, referred to as a "ductility" map, is divided into three behavioral regions: (1) ductile; (2) transitional; and (3) brittle. In the ductile region, ℓ_p is much greater than ℓ_t; that is, plastic relaxation of the pre-existing flaw dominates its behavior. Wing-crack formation would be effectively suppressed (though not completely). In the brittle region, ℓ_t is much greater than ℓ_p. Wing-crack formation dominates the behavior of the pre-existing flaw, with plastic relaxation effectively suppressed. Finally, in the transitional region, ℓ_p is initially greater than ℓ_t, but eventually ℓ_t becomes greater than ℓ_p. That is, initially, plastic relaxation dominates; however, eventually wing-crack formation dominates as a result of increasing load. As can be seen from this figure, increasing ductility Δ and confining stress promotes ductile behavior. Several armor-grade ceramics are also shown in Figure 5(b) assuming plane strain loading conditions (characteristic of the initial shock phase of the ballistic event). Data for SiC, TiB_2, and WC were taken from Shih[31]. It was assumed that 2c equals the average grain size and τ_Y = ½*HEL (HEL = Hugoniot Elastic Limit). Based upon this figure, shock-induced wing-crack formation would be suppressed in SiC, TiB_2, and WC; however, wing-cracks would be expected to grow for B_4C. It must be noted that the ductility map shown in Figure 5(b) was constructed with $\mu = 0.4$. For $\mu < 0.4$, the boundaries would shift up, increasing the size of the brittle region.

For the wing-crack shown in Figure 5(a), assuming that $\gamma = 45^\circ$ and $\ell_t^*/c = 0$, the two governing analytical expressions derived by Horii and Nemat-Nasser[23] become:

$$\Delta = \frac{K_{IC}}{\tau_Y\sqrt{\pi c}} = \frac{\left(\frac{\sigma_1}{\tau_Y}\right)\left[\left(1-\frac{\sigma_2}{\sigma_1}\right)-\mu\left(1+\frac{\sigma_2}{\sigma_1}\right)-\sqrt{2\pi}\left(\frac{\sigma_2}{\sigma_1}\right)\left(\sqrt{\frac{\ell_t}{c}}\right)^2\right]}{\sqrt{2\pi}\sqrt{\frac{\ell_t}{c}}} \quad (1)$$

$$\frac{\sigma_1}{\tau_Y} = -\frac{2\left\{1-\left(\frac{2}{\pi}\right)\sin^{-1}\left[1\Big/\left(1+\frac{\ell_p}{c}\right)\right]\right\}}{\left(1-\frac{\sigma_2}{\sigma_1}\right)-(2\mu/\pi)\left(1+\frac{\sigma_2}{\sigma_1}\right)\sin^{-1}\left[1\Big/\left(1+\frac{\ell_p}{c}\right)\right]} \quad (2)$$

Given that toughened ceramics exhibit R-curve behavior, i.e. increasing fracture toughness with increasing crack extension[32-33], the most appropriate value for K_{IC} is the "short-crack" fracture toughness, where the flaw size on the order of the grain size (i.e. a "natural" flaw and not an "artificial" flaw). Based upon Equations (1) and (2), the relationship between ℓ_p and ℓ_t in terms of Δ, σ_2/σ_1, and μ can be derived. This will not be done in this paper, but the relationship is mentioned to inform the reader that ℓ_p and ℓ_t are not independent. The importance of this relationship is that it places physical limits on the possible values of the governing parameters. For example, the limitation

that $\ell_t/c < 0.5$ places limitations on the possible values for ℓ_t, Δ, σ_2/σ_1, and μ. Equation (1) can be rewritten to give the critical shear stress τ^* ($\tau^* = \frac{1}{2}|\sigma_1 - \sigma_2|$):

$$\frac{\tau^*}{\tau_Y} = \frac{\left(\frac{\pi\Delta}{\sqrt{2}}\right)\left(1-\frac{\sigma_2}{\sigma_1}\right)\sqrt{\frac{\ell_t}{c}}}{1-\mu-\left[1+\mu+\sqrt{2}\pi\left(\frac{\ell_t}{c}\right)\right]\left(\frac{\sigma_2}{\sigma_1}\right)} \tag{3}$$

From Equation (3), another limitation on the governing parameters can be obtained based upon the condition $\tau^*/\tau_Y < 1$. Furthermore, it can be seen that τ^* is dependent upon the local confining stress σ_2 (i.e. failure is pressure dependent). Therefore, in order to utilize Equation (3), an expression for the confining stress must be obtained. For this, we turn to Hertz's contact theory for elastic bodies.

3.2 Impact Stress Distribution

In this model development, the impact stress distribution p(r) is assumed to be that generated by the frictionless contact between two elastic solids of revolution, and is given by[30]:

$$p(r) = p_o\sqrt{1-(r/a)^2} \tag{4}$$

where p_o is the maximum impact stress and a is the contact radius. Based upon this applied stress distribution, the principal stresses and shear stress generated in the elastic solid along the z-axis (center-line) are given by[30]:

$$\frac{\sigma_1^H}{p_o} = -\frac{1}{1+(z/a)^2} \tag{5a}$$

$$\frac{\sigma_2^H}{p_o} = \frac{\sigma_3^H}{p_o} = -(1+\nu)\left[1-\left(\frac{z}{a}\right)\tan^{-1}\left(\frac{a}{z}\right)\right] + \frac{1}{2\left[1+(z/a)^2\right]} \tag{5b}$$

$$\frac{\tau^H}{p_o} = \frac{1}{2}\left|(1+\nu)\left[1-\left(\frac{z}{a}\right)\tan^{-1}\left(\frac{a}{z}\right)\right] - \frac{3}{2\left[1+(z/a)^2\right]}\right| \tag{5c}$$

where ν is the Poisson's ratio of the elastic solid. Equations (5a), (5b), and (5c) are plotted in Figure 6 for $\nu = 0.2$. Also shown is the ratio of confining stress to the normal stress, i.e. $(\sigma_2/\sigma_1)^H$. As can be seen, characteristic of contact, the maximum shear stress occurs below the surface. In the following sections, it is implicitly assumed that to a first-order approximation, the damage does not alter the stress distributions obtained from Hertz's contact theory.

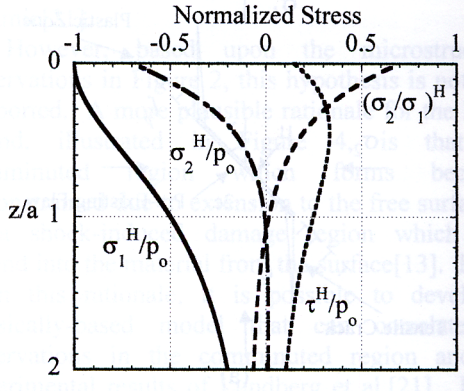

Figure 6. Normalized principal stresses and shear stress along the center-line as a function of normalized depth ($\nu = 0.2$) given by Equation(s) 5.

3.3 Dwell/Penetration Transition Model

It is now possible to construct the physically-based model that can be used to correlate the severity of the damage in the comminuted region, as well as the experimental results of Lundberg et al.[21]. From Equations (3), (5c), (5a), and (5b), the following relationship is obtained:

$$\frac{\tau^H}{\tau^*} = \frac{\left(\frac{p_o}{\tau_Y}\right)}{2\sqrt{2}\pi\Delta\sqrt{\frac{\ell_t}{c}}}\left\{\frac{3-\mu+\sqrt{2}\pi\left(\frac{\ell_t}{c}\right)}{1+(z/a)^2} - 2(1+\nu)\left[1+\mu+\sqrt{2}\pi\left(\frac{\ell_t}{c}\right)\right]\left[1-\left(\frac{z}{a}\right)\tan^{-1}\left(\frac{a}{z}\right)\right]\right\} \tag{6}$$

Equation (6), for values equal to and greater than one, is plotted in Figure 7 showing the effect of varying Δ, μ, and ℓ_t/c ($\nu = 0.2$) for $p_o/\tau_Y = 1$. Based upon the observations in Figure 2, the interaction between and subsequent coalescence of neighboring wing-cracks is artificially introduced by limiting ℓ_t/c to be less than 0.2 instead of 0.5. According to Nemat-Nasser and Deng[24], the interaction between wing-cracks can substantially reduce the

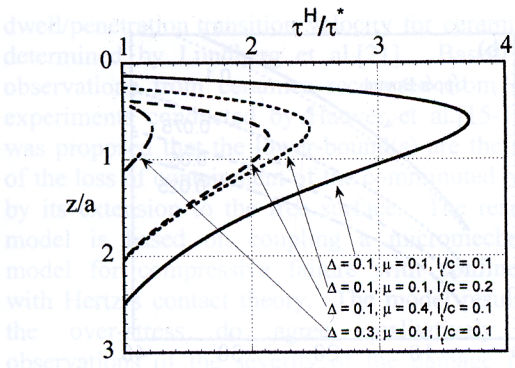

Figure 7. Effect of Δ, μ, and ℓ_t/c (ν = 0.2) on the over-stress τ^H/τ^* for $p_o/\tau_Y = 1$.

failure stress depending upon their initial separation, relative confining stress, and strain-rate (< 10^6 s^{-1}). From Figure 7, the size of and severity of damage within the comminuted region can be qualitatively assessed, in light of Figure 2. For the values of Δ, μ, and ℓ_t/c used in producing Figure 7, several observations can be made with respect to these figures. First, an undamaged region extends into the material from the surface. The extent of this undamaged region increases with increasing Δ, μ, and ℓ_t/c. For sufficiently large Δ, no comminuted region would be expected. Second, if it is assumed that the magnitude of the over-stress is proportional to the severity of the damage, the severity of the damage quickly rises to a maximum within the comminuted region. Lastly, after the maximum, the severity of damage decreases at a slower rate than its initial rise. These three observations are consistent with those seen in Figure 2. While it is acknowledged that an obvious possible limitation of this model is that the stress distributions determined under Hertz's contact theory are limited to elastic bodies, it does provide excellent qualitative agreement with experimental observations.

Equation (6) can be rewritten to give the critical impact pressure p_o^* necessary to expand the comminuted region to the free surface (i.e. $\tau^H/\tau^* = 1$ and z/a = 0):

$$\left(\frac{p_o}{\tau_Y}\right)^* = \frac{2\sqrt{2}\pi\Delta\sqrt{\frac{\ell_t}{c}}}{1-2\nu-(3+2\nu)\mu-\sqrt{2}\pi(1+2\nu)\left(\frac{\ell_t}{c}\right)} \quad (7)$$

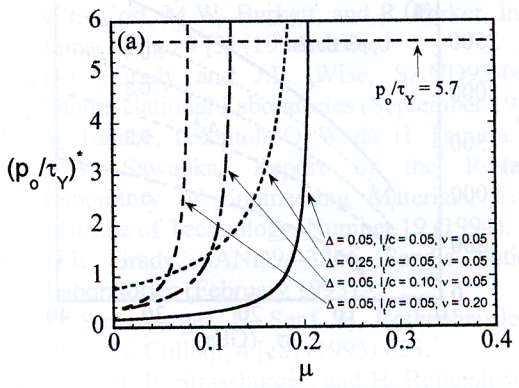

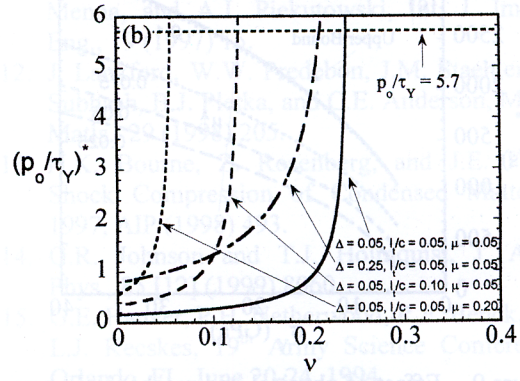

Figure 8. $(p_o/\tau_Y)^*$ as a function of (a) μ, (b) ν, and various values of Δ and ℓ_t/c.

Equation (7) is plotted in Figure 8(a) and 8(b) as a function of μ and ν (fixed Δ and ℓ_t/c), respectively. The orange-dotted line corresponds to the critical pressure ($p_o = 5.7\tau_Y$) required to indent a rigid perfectly-plastic solid as determined from plastic slip-line analysis[30,34]. This value for the critical pressure approximately corresponds to the condition $\tau^* = \tau_Y$. Again, because of the above mentioned limitation of this model, the critical pressures as determined from Equation (7) represent upper-bounds in the pressures necessary to extend the comminuted region to the free surface.

From Lundberg et al.[21], the impact pressure p_o is related to the impact velocity v_p by the relation:

$$v_p = \sqrt{\left(\frac{2K_p}{\rho_p}\right)\left[-1+\sqrt{1+2\left(\frac{p_o-3.27\sigma_{Yp}}{K_p}\right)}\right]} \quad (8)$$

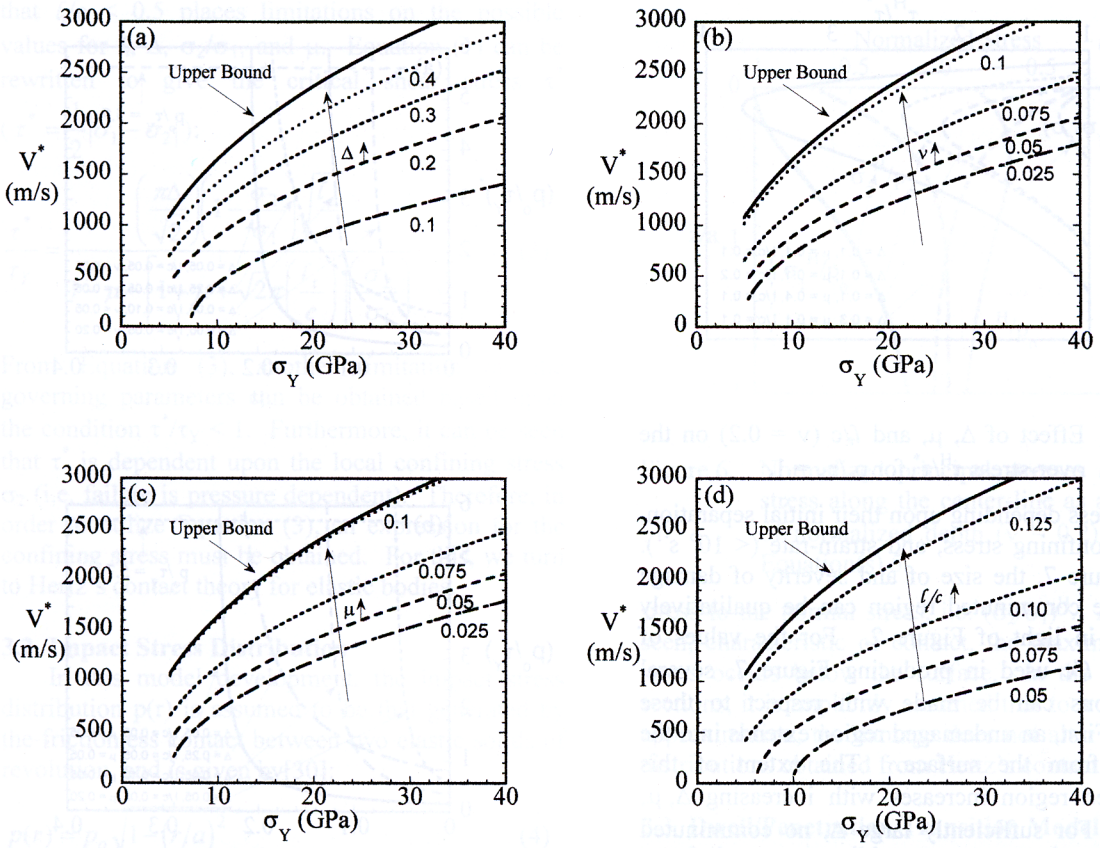

Figure 9. Effect of physical and mechanical parameters on the dwell/penetration transition velocity V* (plotted as a function of yield strength σ_Y): (a) Effect of Δ with $\ell/c = 0.1$, $\nu = 0.05$, and $\mu = 0.05$; (b) Effect of ν with $\Delta = 0.2$, $\ell/c = 0.1$, and $\mu = 0.05$; (c) Effect of μ with $\Delta = 0.2$, $\ell/c = 0.1$, and $\nu = 0.05$; and (d) Effect of ℓ/c with $\Delta = 0.2$, $\nu = 0.05$, and $\mu = 0.05$.

where K_p, ρ_p, and σ_{Yp} are the bulk modulus, density, and yield strength of the projectile material, respectively. The dwell/penetration transition velocity V^* is determined from Equation (8) when $p_o = p_o^*$. V^* is plotted as a function of yield strength in Figures 9(a), 9(b), 9(c), and 9(d) for several values of Δ, μ, ν, and ℓ/c, respectively. As can be seen from these figures, Δ, μ, ν, and ℓ/c (with increasing strain-rate, $\ell/c \rightarrow 0.5$) have a strong effect on V^*. Given the strong effect of any one of these parameters on V^*, it is not possible to ascribe experimental differences in V^* solely to differences in fracture toughness, grain size, and Poisson's ratio. It is possible to increase the fracture toughness of a material, but still end up with a lower performance because of detrimental changes to the other parameters. In order to determine a correlation based upon these parameters, the other parameters (i.e. μ and ℓ/c) must be determined and kept constant (a most difficult proposition). In general, based upon this model, the desirable characteristics for a ceramic are a high yield strength (high hardness), high fracture toughness, high Poisson's ratio, high coefficient of friction, and small grain size (or flaw size). A ceramic possessing this combination of characteristics would exhibit a dwell/penetration transition velocity high on the upper-bound curve shown in Figure 9.

4. SUMMARY AND CONCLUSIONS

A hypothesis has been proposed and a model developed to explain the lower-bound(s) in the

dwell/penetration transition velocity for ceramics as determined by Lundberg et al.[21]. Based upon observations from ceramics recovered from dwell experiments conducted by Hauver et al.[15-16], it was proposed that the lower-bound(s) are the result of the loss of containment of the comminuted region by its extension to the free surface. The resulting model is based on coupling a micromechanical model for compressive failure with confinement with Hertz's contact theory. The model results for the over-stress do agree qualitatively with observations of the severity of the damage in the comminuted region. Based upon the expression derived for the critical pressure to extend the comminuted region to the free surface, the parameters that strongly affected the dwell/penetration transition velocity V^* were τ_Y, Δ, μ, ν, and ℓ/c (note that Δ and ℓ/c are not independent). In developing a ceramic with a high dwell/penetration transition velocity, the effect of the critical parameters must be kept in mind. For example, it is incorrect to focus solely on improving fracture toughness (especially long-crack fracture toughness) without considering how the other critical parameters might be affected. Because Hertz's contact theory is limited to elastic solids, the model results for the critical pressure necessary to extend the comminuted region to the free surface represent possible upper-bounds.

ACKNOWLEDGEMENTS

The authors would like to acknowledge the past support of Mr. George Hauver in sharing his tremendous experimentally-based knowledge on interface defeat. We would also like to thank Dr. Laszlo Kecskes who spent many hours polishing the cross-sections of the recovered ceramics. And finally, we would like to thank Dr. John Beatty, Dr. Andy Wereszczak, and Dr. Jane Adams for their support in reviewing this manuscript.

REFERENCES

1. M.L. Wilkens, C.F. Cline, and C.A. Honodel, "Light Armor," UCRL 71817, July 1969, 71 pp.
2. M.L. Wilkins, Int. J. Eng. Sci., 16 (1978) 793.
3. J. Sternberg, J. Appl. Phys., 65 [9] (1989) 3417.
4. J.E. Field, Q. Sun, D. Townsend, Mechanical Properties of Materials at High Rates of Strain 1989, Proceedings of the Fourth International Conference, (1989), 387.
5. D.A. Shockey, A.H. Marchand, S.R. Skaggs, G.E. Cort, M.W. Burkett, and R. Parker, Int. J. Impact Eng., 9 [3] (1990) 263.
6. D.E. Grady and J.L. Wise, SAND93-0610, Sandia National Laboratories (September 1993).
7. Y. Tanabe, T. Saitoh, O. Wada, H. Tamura, and A.B. Sawaoka, Report of the Research Laboratory of Engineering Materials, Tokyo Institute of Technology, Number 19 (1994).
8. D.E. Grady, SAND94-3266, Sandia National Laboratories (February 1995).
9. E. Strassburger, H. Senf, H. Rothenhausler, J. Phys. IV Colloq., 4 [c8] (1995) 653.
10. H. Senf, E. Strassburger, and H. Rothenhausler, J. Phys. IV Colloq., 4 [c8] (1995) 741.
11. D.L. Orphal, R.R. Franzen, A.C. Charters, T.L. Menna, and A.J. Piekutowski, Int. J. Impact Eng., 19 (1997) 15.
12. J. Lankford, W.W. Predebon, J.M. Staehler, G. Subhash, B.J. Pletka, and C.E. Anderson, Mech. Matls., 29 (1998) 205.
13. N.K. Bourne, Z. Rosenberg, and J.E. Field, Shock Compression of Condensed Matter – 1997, AIP (1998) 493.
14. G.R. Johnson and T.J. Holmquist, J. Appl. Phys., 85 [12] (1999) 8060.
15. G.E. Hauver, P.H. Netherwood, R.F. Benck, and L.J. Kecskes, 19th Army Science Conference, Orlando, FL, June 20-24, 1994.
16. G.E. Hauver, P.H. Netherwood, R.F. Benck, and E.J. Rapacki, ARL Technical Report, in progress.
17. E.J. Rapacki, G.E. Hauver, P.H. Netherwood, and R.F. Benck, 7th Annual TARDEC Ground Vehicle Survivability Symposium, Monterey, CA, March 26-28, 1996.
18. W. Bruchey, E. Horwath, D. Templeton, Proceedings of the 17th International Symposium on Ballistics, Midrand, South Africa, March 1998.
19. H.D. Espinosa, N.S. Brar, G. Yuan, Y. Xu, and V. Arrieta, Int. J. Solids Structures, 37 [36] (2000) 4893.
20. P. Lundberg, L. Holmgren, and B. Janzon, Ballistics'98, Proceedings of the Seventeenth International Symposium on Ballistics, Midrand, South Africa, March 1998, 3 (1998) 251.
21. P. Lundberg, R. Renstrom, and B. Lundberg, Int. J. Impact Eng., 24 (2000) 259.